arXiv:2306.02659v1 [cs.RO] 5 Jun 2023

Hybrid Trajectory Optimization for Autonomous Terrain Traversal of Articulated Tracked Robots

Zhengzhe Xu, Yanbo Chen, Zhuozhu Jian, Xueqian Wang, and Bin Liang

***Abstract*— Autonomous terrain traversal of articulated tracked robots can reduce operator cognitive load to enhance task efficiency and facilitate extensive deployment. We present a novel hybrid trajectory optimization method aimed at generating smooth, stable, and efficient traversal motions. To achieve this, we develop a planar robot-terrain interaction model and partition the robot's motion into hybrid modes of driving and traversing. By using a generalized coordinate description, the configuration space dimension is reduced, which provides real-time planning capability. The hybrid trajectory optimization is transcribed into a nonlinear programming problem and solved in a receding-horizon planning fashion. Mode switching is facilitated by associating optimized motion durations with a predefined traversal sequence. A multi-objective cost function is formulated to further improve the traversal performance. Additionally, map sampling, terrain simplification, and tracking controller modules are integrated into the autonomous terrain traversal system. Our approach is validated in simulation and real-world experiments with the Searcher robotic platform, effectively achieving smooth and stable motion with high time and energy efficiency compared to expert operator control. (Video[1])**

I. Introduction

Mobile robots are revolutionizing a wide range of industries, from emergency response and disaster relief to environmental exploration and infrastructure maintenance [1]–[3]. However, their successful deployment is heavily dependent on the ability to traverse challenging terrain and overcome obstacles with ease. Articulated tracked robots have emerged as a promising solution to these challenges, with large track contact areas providing unparalleled stability and controllable flippers available for support, offering high terrain traversal capabilities. The Searcher robot that we use is an example as shown in Fig.1.

Articulated tracked robots are commonly operated through remote control, a demanding task that requires skilled operators to simultaneously monitor their surroundings while controlling the acceleration, steering, and flipper angles, making stability and efficiency an inherent trade-off. A more efficient approach of terrain traversal is to maintain a specific speed while using an appropriate flipper configuration for support, which utilizes all degrees of freedom (DOFs) simultaneously rather than separated motions. Autonomous execution of such optimized motions offers several benefits, including reducing the cognitive load on human operators and improving task efficiency. Optimization-based planning methods are particularly effective in generating efficient motion. However, the track's contact-rich nature leads to complex contact dynamics, and whether flippers are used for support presents hybrid motion patterns, posing significant planning challenges.

Fig. 1. The *Searcher*, an articulated tracked robot, utilizes flippers to support itself, enabling it to surmount uneven terrain such as high platforms and stairs with ease.

Autonomous terrain traversal requires ensuring robot stability with higher motion smoothness and efficiency than expert operators. To overcome the challenges, we propose a simplified model of the articulated tracked robot interacting with the terrain, performing trajectory optimization based on the predefined traversal sequence to achieve hybrid mode switching, resulting in stable, smooth and efficient motions.

A. Related Work

Autonomous terrain traversal of articulated tracked robots is a long-studied problem. Early studies [4]–[6] have shown that pre-set simple strategies relying on sensor-reflection can achieve this goal. However, these strategies are limited in generating complex motions and may not be applicable to different types of terrain. In recent years, learning-based approaches have been used to address flipper control and autonomous traversal, such as neuroevolution [7] and reinforcement learning [8], [9]. These studies are conducted solely on a single type of terrain, while our work focuses on a general terrain traversal scheme.

Many studies emphasize the significance of flipper configuration in terrain traversal and have defined discrete flipper templates (or shapes, states, postures) that effectively address configuration selection in different terrains. A D*-Lite-based path planning method is proposed in [10], where robot position planning and flipper configuration planning

This work was supported by the National Natural Science Foundation of China under Grant 62293545. *(Zhengzhe Xu and Yanbo Chen are co-first authors.) (Corresponding author: Xueqian Wang.)*

Zhengzhe Xu, Yanbo Chen are with the School of Mechanical Engineering and Automation at Harbin Institute of Technology, Shenzhen 518055, China (e-mail: 200320314@stu.hit.edu.cn; 190320129@stu.hit.edu.cn)).

Zhuozhu Jian, Xueqian Wang, Bin Liang are with the Center for Artificial Intelligence and Robotics, Shenzhen International Graduate School, Tsinghua University, Shenzhen 518055, China (e-mail: jzz21@mails.tsinghua.edu.cn; wang.xq@sz.tsinghua.edu.cn; liangbin@mail.tsinghua.edu.cn).

[1]Video demonstration: `https://youtu.be/GInGuerhCAs`.

are separated. Suitable flipper configurations are selected among the four predefined flipper postures based on the terrain information on the path. Similarly, in [11], five flipper shapes are defined, and a linear classifier is trained to predict the appropriate shape for the terrain. In [12], seven states are defined, and a learnable soft-differentiable neural state machine architecture is proposed that considers the probability of switching between states. However, these approaches do not consider motion smoothness during a whole traversal, which may lead to inefficient motion and high energy consumption due to frequent state switching. In contrast, a continuous traversal sequence is proposed in [5], which enabled cooperation between the front and rear flippers but lacked a unified strategy and clear criteria for specific phases. A simplified robot skeleton model is developed in [13], [14], and continuous motion is generated by searching a reduced-dimensional configuration space, However, their approach prioritizes the transitions between adjacent configurations over overall motion efficiency.

Optimization-based motion planning enables the generation of intricate robot motions, as demonstrated by trajectory optimization (TO) techniques in enhancing mobility for legged robots [15]–[17]. TO have proven effective in improving the robot locomotion in various scenarios. For instance, a whole-body trajectory planning for walking excavators to achieve statically stable motion in rough terrain [18], focusing on kinematically feasible motions. Furthermore, the hybrid trajectory optimization (HTO) method has been utilized to generate multi-phase motions for hybrid systems with discontinuous dynamics [19], [20].

For our Searcher robot, which weighs over 200kg and has a considerable touchdown area providing sufficient friction, we focus on kinematically feasible solutions to maintain static equilibrium. However, the contact-rich nature of tracked robots poses a significant challenge, rendering the task of developing a robot-terrain interaction (RTI) model accessible for planning arduous. Previous studies analyze the interaction between this type of robot and the terrain [21], [22], but the model complexity impedes effective planning.

B. Contributions

This work offers the following contributions:

- We propose a planar RTI model for articulated tracked robots to simplify the contact patterns. The configuration space is reduced to three dimensions by generalized coordinates, facilitating real-time planning capabilities.
- We develop a novel HTO formulation to generate terrain traversal motions with mode switching. By formulating a multi-objective cost function, we improve motion efficiency, smoothness, and stability.
- We integrate the map sampling, terrain simplification, and tracking controller modules into a terrain traversal system. The system is validated using the Searcher robotic platform in both simulation and real-world scenarios, comparing it with expert operator control and demonstrating smoother motion, greater stability, and higher time and energy efficiency.

II. Modeling

A. Planar Robot-Terrain Interaction Model

The Searcher has coaxial left and right flippers, indicating its suitability for traversing terrain with little undulation in the longitudinal section. Therefor, the RTI model is developed in the longitudinal plane to obtain a reduced configuration description through the interaction between a simplified terrain and robot model.

1) Simplified Terrain Model: Due to the large contact area provided by the track, the robot can traverse terrains with low undulation and unevenness without relying on the support of flippers. This insight motivates us to simplify the terrain into simple planes that are represented in two dimensions by line segments as shown in Fig. 2(a). The simplified terrain set is defined as $\mathbb{T} = \{\tau_i\}_{i=1}^{N_t}$, where the terrain τ_i is described by the start and end point of the line segment. Each terrain can be parameterized by the inclination α, height h and length ℓ. α is the angle of the terrain with respect to the horizontal plane. h is the vertical distance between the endpoint of the upper terrain and the lower one, with positive values indicating an increase in elevation, and the height of the last terrain set to 0. ℓ is the line segment length.

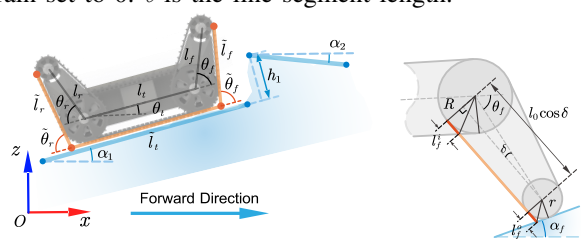

Fig. 2. Illustration of the simplified models. The flipper length $l_f = l_r = l_0$ and the track length l_t are indicated in Fig. 2(a). θ_f and θ_r denote the front and rear flipper angles, θ_t is the pitch angle (set the robot head up as positive). The symbols with tilde indicate the model parameters. Fig. 2(b) shows the front flipper as an example of a model flipper length consisting of a fixed-length part $l_0 \cos\delta$ and two variable-length parts $l_{\tilde{f}}^i$ and $l_{\tilde{f}}^o$.

2) Simplified Robot Model: For robots with flippers of different gear diameters, the skeleton model proposed in [13] cannot accurately capture the contact with the terrain. To overcome this limitation, we introduced a planar model with the bottom surface of the robot represented by three time-varying rods, as shown in Fig.2(a). We use the shorthand notation of $(\cdot)_{f,r}$ to denote the parameters of the front and rear flippers, respectively. The angle of the model flippers is calculated by $\tilde{\theta}_{f,r} = \theta_{f,r} + \delta$, where $\delta = \arcsin((R-r)/l_0)$ is the angle caused by the gear diameter difference. This simplification approximates the arc at the large gear as a fold, and the error can be neglected when the flipper angle is small. Furthermore, we extended the flipper length for capturing the outer end of the flippers in contact with the terrain, as depicted in Fig. 2(b). Specifically, we have $\tilde{l}_{f,r} = l_{f,r}\cos\delta + l_{f,r}^i + l_{f,r}^o$ and $\tilde{l}_t = l_t + l_f^i + l_r^i$, where

$$\begin{cases} l_{f,r}^i = R\tan\left(\tilde{\theta}_{f,r}/2\right) \\ l_{f,r}^o = \max\left\{r\tan\left(\left(\tilde{\theta}_{f,r} \mp (\theta_t + \alpha_{f,r})\right)/2\right), 0\right\} \end{cases} . \quad (1)$$

For simplicity, we use symbols without tilde to represent the parameters of the robot model in the subsequent sections.

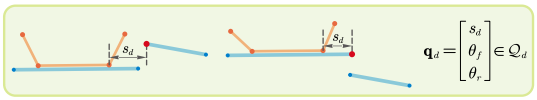

(a) Definition of s_d at ascent and descent.

(b) Definition of s_t at ascent and descent.

Fig. 3. Definitions of the generalized coordinates and configuration description, with the robot traveling from left to right. Support points are marked with red dots. Direction of increasing s_t is indicated by the dashed arrows.

3) Configuration Space Reduction: The robot state in the 2D plane can be expressed as $\bar{\mathbf{q}}=\begin{bmatrix} x & z & \theta_t & \theta_f & \theta_r \end{bmatrix}^\top \in \mathbb{R}^5$, where (x, z) denotes the position of body center. During terrain traversal, the interaction between the robot and the terrain model involves at least two contact points, which reduces the effective DOFs. We refer to the traversal as ascending when the robot traverses adjacent terrains with $h > 0$, and as descending when $h < 0$. When ascending, the support point is defined as the starting point of the next terrain, and when descending, it is defined as the end point of the current terrain, which is illustrated in Fig. 3. When the robot's track is attached to the ground, we define the projection of the support point on the current terrain from the front end of the track as the coordinate s_d, and the robot state is reduced to $\mathbf{q}_d=\begin{bmatrix} s_d & \theta_f & \theta_r \end{bmatrix}^\top \in \mathcal{Q}_d \subset \mathbb{R}^3$, as shown in Fig. 3(a). When the robot contacts the support point, we describe its configuration by the generalized coordinate of the distance s_t that the support point has moved over the robot planar model, and the state is $\mathbf{q}_t=\begin{bmatrix} s_t & \theta_f & \theta_r \end{bmatrix}^\top \in \mathcal{Q}_t \subset \mathbb{R}^3$, as shown in Fig. 3(b). $\mathcal{Q}_d$ and $\mathcal{Q}_t$ are driving and traversing configuration spaces, respectively, describing the model state in the two hybrid modes (to be defined in Sec. II-B).

B. Hybrid Mode Definition and Traversal Sequence

In this part, we first introduce a stable traversal strategy, then define two hybrid modes based on contact and propose a traversal sequence for HTO. This strategy makes full use of the support of the flippers in traversal, as depicted in Fig. 4. Specifically, during ascent (along the yellow arrows), the front flipper spreads to attach to the support point and then climbs up. Then, the rear flipper supports the lower terrain, while the front flipper supports the higher one, ensuring robot stability until the center of mass (COM) reaches a higher terrain. Once the COM enters the higher terrain, the robot can lift the flippers and drive forward to complete the traversal. During descent (along the red arrows), the rear flipper supports to maintain a specific body inclination. This enables the front flipper to support the lower terrain, allowing the robot to drive and descend.

Based on the contact of the flippers, we can define two hybrid modes: *driving mode* and *traversing mode*. In ascent, traversing mode starts when the front flipper attaches the support point until the COM reaches a higher terrain and then the rear flipper is able to detach from the lower terrain; in descent, it starts when the front flipper attaches the lower terrain and ends when the rear flipper is detached from the higher terrain. In addition, the robot is considered to be in driving mode, which implies that it can drive without adjusting flippers. When using the symbol $\mathbf{q}$, its meaning $\mathbf{q}_d$ (driving) or $\mathbf{q}_t$ (traversing) depends on the current mode.

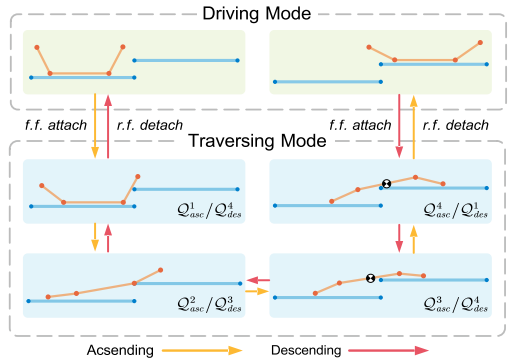

Fig. 4. Illustration of our stable traversal strategy for ascent and descent, involving switching between driving mode and traversing mode. The lower four key nodes form the traversal sequence, counterclockwise for the ascending S_{asc} and clockwise for the descending S_{des}. The abbreviation *f.f.* and *r.f.* are for the front flipper and rear flipper.

The concept of traversal sequence was first proposed in [5], but lacked a consistent formulation guideline. We propose a uniform guideline for this sequence to function similarly to the contact schedule of legged robots. A traversal sequence can be denoted as $S = \left(\mathcal{Q}^1, \cdots, \mathcal{Q}^{N_s}\right)$, where $\mathcal{Q}^i \subset \mathcal{Q}_t$ and s_t^i increases. It includes N_s constrained traversal configuration space key nodes that the robot must pass through during traversal, and the generalized coordinates s_t are sequentially increasing. We developed a traversal sequence with $N_s = 4$, as shown in the four ordered blocks at the bottom of Fig. 4. Based on the symmetry of the robot configuration, the ascending sequence $S_{asc} = \left(\mathcal{Q}^1_{asc}, \mathcal{Q}^2_{asc}, \mathcal{Q}^3_{asc}, \mathcal{Q}^4_{asc}\right)$ and the descending sequence $S_{des} = \left(\mathcal{Q}^1_{des}, \mathcal{Q}^2_{des}, \mathcal{Q}^3_{des}, \mathcal{Q}^4_{des}\right)$ are naturally designed as symmetric processes, which is useful when formulating configuration descriptions.

The configuration descriptions for $\mathcal{Q}^i_{asc}$ can be derived geometrically, as shown in Table I, where s_t^{com} is the COM position expressed in generalized coordinate s_t. For the simplicity of derivation, α and h here are the relative inclination and height between the two terrains, respectively. We use $(\cdot)_u$ and $(\cdot)_l$ to denote the upper and lower bounds.

By utilizing the symmetry of the robot configuration and the sequence, we do not need to re-derive the descending configuration description. We define the dual traversing configuration as $\mathbf{q}_t^* = \begin{bmatrix} l_\Sigma - s_t & \theta_r & \theta_f \end{bmatrix}^\top$, where $l_\Sigma = l_f + l_t + l_r$. This can be considered as the forward direction of the robot being flipped. Additionally, the parameters in the ascending configuration $\mathcal{Q}_{asc}$ are replaced with their dual counterparts, which involves swapping l_f and l_r, θ_f and θ_r, and s_t^{com} and $l_\Sigma - s_t^{com}$ to obtain the dual description $\mathcal{Q}^*_{asc}$. As a result, the descending configuration $\mathbf{q}_t \in \mathcal{Q}^i_{des}$ can be described by $\mathbf{q}_t^* \in \left(\mathcal{Q}^{5-i}_{asc}\right)^*$.

Additionally, for the special case of $h = 0$, we adopt the descending description when $\alpha < 0$, as it is compatible with the descending strategy. For $\alpha > 0$, we can introduce a height of $h_\delta > 0$ to adopt the ascending description.

TABLE I: Configuration Descriptions On Key Nodes During Ascending

Node	Configuration Description	
$\mathcal{Q}_{asc}^1$	$0 < s_t < l_f$	$(l_f - s_t)\sin\theta_f = h$ $0 \le \theta_r \le \theta_u$
$\mathcal{Q}_{asc}^2$	$s_t = l_f$	$l_t \sin\theta_t + l_r \sin(\theta_t - \theta_r) = h$ $\theta_{t,l} \le \theta_t \le \theta_{t,u}$ $\theta_t - \alpha \le \theta_f \le \theta_u$ $\theta_l \le \theta_r \le \theta_t$
$\mathcal{Q}_{asc}^3$	$l_f < s_t < s_t^{com}$	$(s_t - l_f)\sin(\theta_t - \alpha)$ $+l_r \sin(\theta_t + \theta_f - \alpha) = 0$ $(l_t + l_f - s_t)\sin\theta_t$ $+l_r \sin(\theta_t - \theta_r) = h$ $\alpha \le \theta_t \le \theta_{t,u}, \theta_l \le \theta_r \le \theta_t$
$\mathcal{Q}_{asc}^4$	$s_t^{com} \le s_t < l_f + l_t$	

III. Hybrid Trajectory Optimization

A. Problem Formulation

We formulate the HTO problem for terrain traversal with the multi-objective cost function ((2a), see Sec. III-D)) weighted by $\lambda_i (i = 1, 2, 3)$, and constraints ((2b)-(2f), see Sec. III-C). The objective is to obtain the trajectory $\{s_d(t), s_t(t), \theta_f(t), \theta_r(t)\}$. The periods when the robot is driving and traversing are denoted as $\mathcal{T}_d$ and $\mathcal{T}_t$, respectively, with t_S and t_T representing the moment of mode switching and the end of the planning horizon respectively.

$$\min \quad J = \lambda_1 J_{time} + \lambda_2 J_{stab} + \lambda_3 J_{smo} \tag{2a}$$

$$\text{s.t.} \quad \text{initial state}: \mathbf{q}(0) = \mathbf{q}_0, \dot{\mathbf{q}}(0) = \dot{\mathbf{q}}_0 \tag{2b}$$

$$\text{terminal state}: \mathbf{q}(t_T) = \mathbf{q}_T \tag{2c}$$

$$\text{configuration} \begin{cases} \mathbf{q}(t \in \mathcal{T}_d) \in \mathcal{Q}_d \\ \mathbf{q}(t \in \mathcal{T}_t) \in \mathcal{Q}_{asc}, \quad \text{for asc.} \\ \mathbf{q}^*(t \in \mathcal{T}_t) \in \mathcal{Q}_{asc}^*, \text{for des.} \end{cases} \tag{2d}$$

$$\text{motion}: \dot{\mathbf{q}}(t) = \mathbf{u} \in \mathcal{U} \tag{2e}$$

$$\text{switching}: \begin{cases} \Delta_c(\mathbf{q}^-(t_S), \mathbf{q}^+(t_S)) = 0 \\ \Delta_m(\mathbf{q}^-(t_S), \mathbf{q}^+(t_S)) \le 0 \end{cases} \tag{2f}$$

Compared to the shooting approach [23] with fixed time steps to plan the hybrid motion, we adopt the direct collocation method [24] to transcribe HTO into a nonlinear programming (NLP) problem, while planning the duration between nodes with less computational complexity. Since the traversal sequence is predefined and the hybrid mode is time-dependent switching, the decision variables are set to the node state $(\mathbf{q}_k, \dot{\mathbf{q}}_k)$, as well as the durations $T_{d,i} (i = 1, \cdots, n_d - 1)$, $T_{t,j} (j = 1, \cdots, n_t - 1)$. The continuous time trajectory is a piecewise cubic polynomial curve, generated by Hermite interpolation.

B. Receding-Horizon Planning Schedule

Since the robot model possesses time-varying parameters (l_f, l_t, l_r), we adopt a receding horizon to replan the trajectory in real time, incorporating the updated parameters to guarantee kinematic feasibility. During the driving mode, the ending node of this traversal is set to the terminal node of the planning horizon (Fig. 5(a)). During the traversal mode, the planning horizon starts from this moment until the end of the next driving period (if it exists) as the terminal node, which predicts the initial state of the next traversal (Fig. 5(b)).

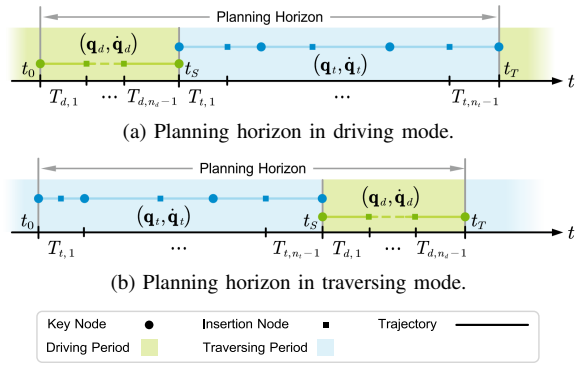

Fig. 5. The planning horizon varies according to the robot's mode. The key nodes in the traversal sequence are represented by circular dots. Meanwhile, additional insertion nodes can be added, depicted by square dots, and have geometrically derived configuration constraints. Insertion nodes influence the trajectory trend and affect the scale of the problem.

C. Constraints

To ensure that the robot follows the predefined traversal sequence, we impose configuration constraints at each node. The motion feasibility is guaranteed by the motion constraints. Moreover, we enforce switching constraints for mode transitions.

1) Configuration Constraints: At the key nodes of the driving mode, we enforce the track to be fit to the ground, and the flippers are constrained to be above ground, with the configuration described as $\mathcal{Q}_d = \{\mathbf{q}_d \mid 0 \le \theta_{f,r} \le \theta_u\}$. The traversing mode configuration constraints are derived geometrically, as given in Table I, with the pitch angle θ_t introduced as an auxiliary variable. For the descent, we impose the dual constraints on its dual configuration $\mathbf{q}^*$.

2) Motion Constraints: To ensure the motion feasibility, we apply (2e) to bound the nominal input $\mathbf{u} = \dot{\mathbf{q}}(t)$, where $\mathcal{U} = \{\mathbf{u} \mid 0 \le v \le v_u, \omega_l \le \omega_{f,r} \le \omega_u\}$ and $\omega_{f,r}$ denotes the flipper velocities, and the nominal velocity v is defined as:

$$v = \begin{cases} -\dot{s}_d, & \text{if } \mathbf{q} \in \mathcal{Q}_d \\ \dot{s}_t, & \text{if } \mathbf{q} \in \mathcal{Q}_t \end{cases}. \tag{3}$$

3) Switching Constraints: We associate the predefined traversal sequence with durations to describe the mode switching events, and determine the switching moment t_S by optimizing durations under the switching constraints. At $t = t_S$, the pre- and post-switch states $\mathbf{q}^-$ and $\mathbf{q}^+$ are in different modes. Therefore, we impose configuration and motion constraints to implement the transition. The configuration switching constraint function from driving to traversing is formulated through geometric relations as follows:

$$\Delta_c(\mathbf{q}^-, \mathbf{q}^+) = \begin{cases} (l_f - s_t)\cos\theta_f - s_d, \text{if } \mathbf{q}^- \in \mathcal{Q}_d, \mathbf{q}^+ \in \mathcal{Q}_{asc}^1 \\ (l_f - s_t)\cos\theta_t - s_d, \text{if } \mathbf{q}^- \in \mathcal{Q}_d, \mathbf{q}^+ \in \mathcal{Q}_{des}^1 \end{cases}. \tag{4}$$

The motion switching constraint considers the velocity loss. We formulate this function from driving to traversing as follows:

$$\Delta_m(\mathbf{q}^-, \mathbf{q}^+) = \begin{cases} \dot{s}_t + \dot{s}_d \cos\theta_f, \text{if } \mathbf{q}^- \in \mathcal{Q}_d, \mathbf{q}^+ \in \mathcal{Q}_{asc}^1 \\ \dot{s}_t + \dot{s}_d \cos\theta_t, \text{if } \mathbf{q}^- \in \mathcal{Q}_d, \mathbf{q}^+ \in \mathcal{Q}_{des}^1 \end{cases}. \tag{5}$$

The functions for traversing to driving are also formulated through a similar derivation.

D. Cost Function

The multi-objective cost function combines time, stability, and smoothness costs, to produce an optimized trajectory prioritizing efficiency, stability, and smoothness.

1) Time Cost: To minimize the time required for traversal, we formulate the time cost as follows:

$$J_{time} = \sum_{i=1}^{n_d-1} T_{d,i}^2 + \sum_{i=1}^{n_t-1} T_{t,i}^2. \tag{6}$$

2) Stability Cost: The stability cost, inspired by the strategy selector in [25], enables the robot to adjust its flipper configurations based on terrain conditions for maintaining stability. For example, in sparse terrains such as stairs, the flippers tend to flatten to increase contact area; whereas in dense terrains, the flippers can lift to balance motor workload and ensure stability. We formulate this cost as follows:

$$J_{stab} = \sum_{i=1}^{n_d+n_t-1} \left(w_{f,i} \left(\theta_{t,i} + \theta_{f,i} - \alpha_{f,i}\right)^2 + w_{r,i} \left(\theta_{t,i} - \theta_{r,i}\right)^2 \right), \tag{7}$$

where α_f takes 0 in driving mode and the relative angle α in traversing mode. It calculates the weighted sum of squares of the angles of the front and rear flippers with respect to the terrain they respectively lie on. The weights w_f and w_r depend on the terrain sparsity, which will be defined in Sec. IV-B. Considering the sparsity c_1 and c_2 of the current terrain and the target terrain, we have $w_r = c_1$ and w_f as follows:

$$w_f = \begin{cases} c_1, & \text{if } \mathbf{q} \in \mathcal{Q}_d \\ 0, & \text{if } \mathbf{q} \in \mathcal{Q}_{asc}^1 \text{ or } \mathbf{q} \in \mathcal{Q}_{des}^4 \\ c_2, & \text{if } \mathbf{q} \in \mathcal{Q}_{asc} \backslash \mathcal{Q}_{asc}^1 \text{ or } \mathbf{q} \in \mathcal{Q}_{des} \backslash \mathcal{Q}_{des}^4 \end{cases}. \tag{8}$$

3) Smoothness Cost: The smoothness cost is used to ensure the interpolated trajectory is smoother and to avoid the back-and-forth motion of the robot and the flippers, which we formulate as follows:

$$J_{smo} = \sum_{\mathbf{q_i} \in \mathcal{Q}_d, \mathcal{Q}_t} \left(\left\| \bar{\dot{\mathbf{q}}}_i - \dot{\mathbf{q}}_i \right\|_{\mathbf{Q}_s}^2 + \left\| \bar{\dot{\mathbf{q}}}_i - \dot{\mathbf{q}}_{i+1} \right\|_{\mathbf{Q}_s}^2 \right), \tag{9}$$

where $\|\mathbf{x}\|_{\mathbf{Q}} := \sqrt{\mathbf{x}^\top \mathbf{Q} \mathbf{x}}$. The average rate of change is computed by $\bar{\dot{\mathbf{q}}}_i = \left(\mathbf{q}_{i+1} - \mathbf{q}_i\right)/T_i$ and $\mathbf{Q}_s$ is a positive-definite weight matrix. This cost term penalizes large changes in velocity and flippers' angular velocity in the trajectory.

IV. Terrain Traversal System

A. Overview

Our proposed terrain traversal system comprises four modules: map sampling, terrain simplification, hybrid trajectory optimization, and tracking controller. Fig. 6 provides a schematic overview of the workflow for terrain traversal.

B. Terrain Simplification

To obtain simplified terrains, we use a set of line segments $\mathbb{T}$ to *cover* a set of sampled points $P = \{p_i = (d_i, h_i)\}_{i=1}^N$. To achieve it, we transform the problem into an optimal path problem of graph theory.

The edge of the terrain provides vital support to a robot during traversal, and large errors in the edge points of the simplified terrain are unacceptable. Therefore, we choose the

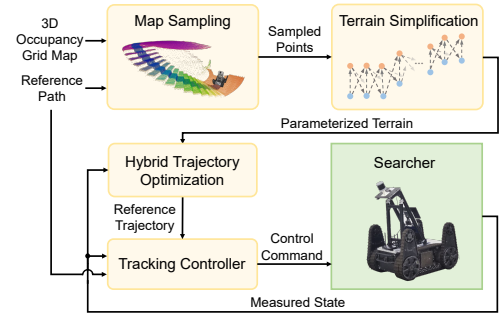

Fig. 6. Workflow of the terrain traversal system. The map sampling module operates on a 3D occupancy grid map and samples each waypoint along the normal of the reference path to obtain a sampled strip. Subsequently, the sampled strip is filtered on the normal to mitigate the effects of map sparsity and random noise. Afterwards, the mean height of each normal is projected onto the distance-height plane, generating a point set P, which is then passed to the terrain simplification module (Sec. IV-B). The resulting simplification is sent to the HTO module. The robot states, which include position, velocity, flipper angles and velocities, and contact situation, are sent to the HTO module. Finally, the tracking controller (Sec. IV-C) utilizes the reference path and trajectory to generate control commands.

start and end points of the line segments to be the points in P, denoted as $\tau_{s,e} = (p_s, p_e), d_s < d_e$. The line segment needs to cover the points in its range, *i.e.*, for any $p_i \in P$ and $d_s \leq d_i \leq d_e$, there is $dist(p_i, \tau_{s,e}) = \frac{p_s p_e \times p_s p_i}{\|p_s p_e\|} \leq \delta_m$, where δ_m is the maximum height difference that the robot can tolerate in driving mode. p_i is considered to be within $\tau_{s,e}$ when $|dist(p_i, \tau_{s,e})| \leq \delta_l$. To prevent the omission of large potholes, the distance between two adjacent points within $\tau_{s,e}$ should not exceed $l_t/2$. The number of points within $\tau_{s,e}$ is $PN(\tau_{s,e})$, and the sparsity is $c(\tau_{s,e}) = 1 - \frac{PN(\tau_{s,e})}{(d_e - d_s)/d_r + 1} \in [0, 1]$, where d_r is the map sampling resolution. Greater sparsity means greater morphological differences between the simplified terrain and the actual terrain. We define the set of all simplified terrains that the robot can traverse as $\mathbb{T}^* = \left\{\tau_{s,e}^*\right\}$ and aim to find the optimal coverage $\mathbb{T} \subset \mathbb{T}^*$ by covering the sampled points using the fewest terrains while keeping as many points within the terrains as possible.

We construct a weighted directed graph $G(V, E)$ with $2N$ vertices. $V = \{v_{2i-1}, v_{2i}\}_{i=1}^N$, where each vertex v_{2i-1} and v_{2i} corresponds to using p_i as the start and end points of a line segment. The edge set E ensures that each path from v_1 to v_{2N} corresponds one-to-one to a subset of $\mathbb{T}^*$, where the cost of a path is the number of terrains in its corresponding subset, and the reward is the sum of the number of sampled points within all terrains in the subset. We use $E_{s \to e} = \left\{(v_{2s-1} \to v_{2e}) \mid \forall \tau_{s,e}^* \in \mathbb{T}^*\right\}$ to denote simplified line segment candidates, which have an edge cost of 1 and reward of $PN(\tau_{s,e}^*)$. To ensure connectivity, we add auxiliary edges $E_{e \to s} = \left\{\left(v_{2i}, v_{2(i+j)-1}\right) \mid 1 \leq i \leq N-1, 0 \leq j \leq N_{ign}\right\}$, where N_{ign} denotes the number of ignored points. These edges connect the endpoint of the previous line segment with the start point of the next line segment. The cost of these edges is 0 because they do not represent simplified line segments. When $j = 0$, two adjacent line segments are directly connected, and the edge rewards are -1 to avoid double counting of the same point. When $j > 0$, the distance between the two line segments does not exceed

$N_{ign} \cdot d_r$. This approach enables the algorithm to ignore noise that may occur between adjacent planes with large height differences on the map, thus improving its robustness. The edge reward for this kind of edge is 0. Finally, we use Dijkstra's algorithm to obtain the optimal terrain coverage.

C. Tracking Controller

The tracking controller is designed to follow both the trajectory generated by HTO and the reference path. The flipper velocity commands are calculated from the reference angles (the model flipper angles are converted to real angles) using the PD control law $\omega_{f,r} = K_p e_{\theta_{f,r}} + K_d e_{\omega_{f,r}}$, where $e_{(\cdot)}$ denotes the deviation between desired and measured.

The nominal velocity input can be computed using the trajectory of generalized coordinates, based on (3). It is essential to ensure that the robot's yaw angle aligns with the reference path while following the nominal velocity. To achieve this, we calculate the robot's angular velocity ω by using the control law in (10). The velocity input (11) is a combination of the nominal velocity feed-forward v^{des} and position feedback. The deviation e_s from the generalized coordinates while driving needs to be taken as the opposite, since s_d decreases.

$$\omega = K_p^{\phi} e_{\phi} + K_d^{\phi} \dot{e}_{\phi}, \tag{10}$$

$$v = v^{des} + K_p^{s} e_s + K_i^{s} \int_0^t e_s(\tau)\, \mathrm{d}\tau. \tag{11}$$

Finally, the track velocity input (v_l, v_r) is determined by (v, ω) through the differential vehicle inverse kinematics.

V. Experiments and Results

We conduct experiments in both simulation and real-world scenarios to verify the effectiveness of our work. The NLP problem for HTO is formulated in CasADi [26] and solved using Ipopt [27]. A priori 3D occupancy grid map with a resolution of 0.02m and a predefined reference path are used in simulations and real-world experiments. We utilize FAST-LIO2 [28] for localization by combining LiDAR scans with IMU data. The optimization nodes number is set to $n_t = 5$ and n_d is determined by the terrain length divided by 0.5m, which ensures real-time planning (computation time within 150ms). The reference trajectory is interpolated to 100Hz for execution. The fast simulation [29] allows us to conduct simulations of Searcher in Gazebo. Fig. 7 shows the Searcher platform for real-world experiments.

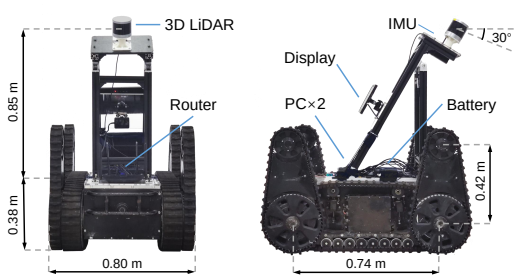

Fig. 7. The Searcher is equipped with the RS-Helios 5515 32-beam LiDAR and IMU. Two Intel NUC 8 (i7-8559U CPU@2.70GHz, 32GB RAM) are used, one for state estimation and the other for planning and control.

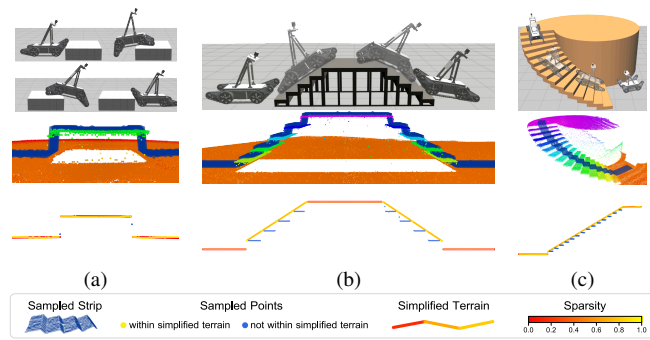

Fig. 8. Screenshot of the simulation experiments and results of map sampling and terrain simplification. (a) A high platform of 0.4m in height and 1.2m in length; (b) Straight stairs ascending and descending with each step 0.2m in height and 0.3m in width; (c) Spiral stairs with a radius of 3.8m, each step 0.2m in height and 0.38m in average width.

A. Comparison of Autonomous Traversal and Operator Control in Typical Terrains

This experiment aims to compare the traversal performance of autonomous terrain traversal (auto.) and expert operator control (oper.) in typical terrains as shown in Fig. 8 to verify the effectiveness of the HTO approach in terms of motion efficiency, smoothness, and stability. The high platform and straight stairs are used to evaluate the effectiveness of the method in traversing obstacles with heights close to the flipper length and on sloping, sparse terrain, respectively. Fig. 8 displays the results of map sampling and terrain simplification, where the simplified terrains of the stairs have high sparsity. The experiments on the spiral stairs demonstrate that the planar RTI model and the planning method are still effective by tracking yaw when the reference path is curved.

To quantitatively compare the traversal quality of auto. and oper., four metrics are proposed and evaluated: (i) total time for terrain traversal; (ii) maximum absolute pitch angle (max $|\theta_t|$). The greater it is, the more likely the robot will tip over; (iii) maximum instantaneous absolute pitch angle velocity (max $|\dot{\theta}_t|$). A greater value implies intense swings and low stability of the robot; (iv) sum of accumulated absolute rotation angles of the front and rear flippers (rot. ang.) which represent the motion smoothness and energy consumption.

We conduct five oper. and auto. trials in each scenario, and compute the average metrics. Identical initial and goal positions are set for each scenario. The results are presented in Table II.

TABLE II: Results of Autonomous Traversal Versus Operator Control

Scene	Method	Time (s)	Max $\lvert\theta_t\rvert$ (°)	Max $\lvert\dot{\theta}_t\rvert$ (°/s)	Rot. Ang. (°)
High Platform	Oper.	**43.73**	19.29	21.39	560.38
	Auto.	45.61	**16.86**	**15.09**	**484.26**
Straight Stairs	Oper.	75.85	35.47	20.94	721.15
	Auto.	**69.32**	**35.18**	**15.17**	**617.06**
Spiral Stairs	Oper.	104.46	32.34	24.53	566.08
	Auto.	**87.51**	**31.90**	**21.06**	**522.18**

The platform and straight stairs are simple terrains, which enables easy observation of ground-robot contact. Expert operators can focus on flipper adjustments while maintaining

Fig. 9. Screenshot of one real-world experiment with multiple terrains, with a total distance of about 24m. The robot needs to first pass through a platform with a height of 0.3m (28s), then traverse six steps (0.16m high and 0.3m wide) (57s and 75s), and climb down four steps of the same size (136s) to reach the ground (150s) after turning in the corridor.

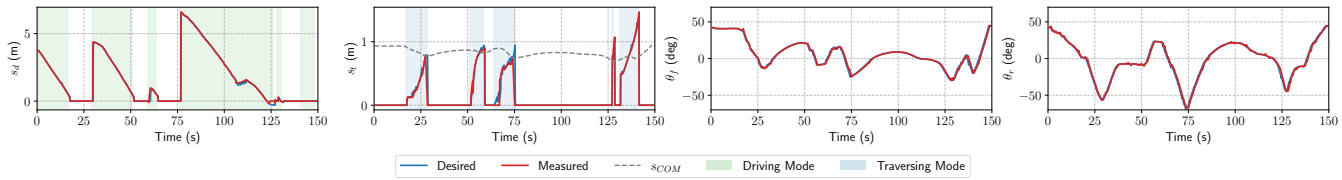

Fig. 10. The planned trajectory $\{s_d(t), s_t(t), \theta_f(t), \theta_r(t)\}$ and the corresponding measurement for the traversing mode period and driving mode period are shaded in blue and green, respectively (the measured s_t for driving and s_d for traversing are set to 0). When the s_t curve is higher than s_t^{com}, the robot in traversing mode is stable on the next terrain. During the 108-113s when the robot is turning, the trajectory is continuously replanned, resulting in a brief increase in s_d. The last driving mode period has no s_d because the robot has already reached the goal terrain and decelerated without planning.

high forward speed with a similar traversal time to the auto. However, steering on spiral stairs brings special contact situations (diagonal flippers contact while the other does not), and improper control can cause the robot to swing or even get stuck during climbing. Additional steering control increases the difficulty of control, and the operator tends to reduce the speed, resulting in increased traversal time. Conversely, autonomous control offers significant advantages.

The traversal strategies of auto. and oper. in these terrains are similar, resulting in comparable max $|\theta_t|$. However, expert operators often struggle to ensure precise control of flipper angles while the robot is moving forward at high speed. They are also prone to larger swings when the COM reaches the next terrain and excess flipper adjustment movements, resulting in a higher max $|\dot{\theta}_t|$ and rot. ang. Overall, our approach offers smoother, more stable motion and is efficient in terms of time and energy consumption.

B. Evaluation of Multi-Objective Cost Function

To evaluate the effectiveness of the cost function, we conduct experiments on straight stairs, analyzing the impact of time, stability, and smoothness costs on HTO through separate removals, with five trials conducted for each removal. After removing the time cost, the robot can not traverse the stairs and remain stationary, as minimizing the time cost incentive drives the robot forward. The average values of the four aforementioned metrics for removing the other two cost terms are shown in Table III.

TABLE III: Effects of Cost Terms on the Straight Stairs

Cost Term	Time (s)	Max $\|\theta_t\|$ (°)	Max $\|\dot{\theta}_t\|$ (°/s)	Rot. Ang. (°)
w/o stab. cost	84.23	35.00	15.87	659.47
w/o smo. cost	72.62	36.71	22.74	640.79

When we remove the stability cost, the robot is no longer flat on the simplified terrain of the stairs. Instead, the extra motion of the flippers causes their endpoints to contact with the steps. This not only increases the rot. ang. and traversal time compared to the full cost function (auto.) in Table II, but it can also result in the robot getting stuck while ascending and falling vertically during the descent. To quantify the fall, we record the maximum z-axis acceleration of the traversal. Without the stability cost, it exceeds the normal range of 0.6-0.7 $\mathrm{m/s^2}$, reaching 1.7 $\mathrm{m/s^2}$. Such a fall can significantly impact the joints due to the robot's substantial weight, leading to damage to the mechanism and motors. Therefore, this cost is both necessary and effective for enhancing motion stability.

When the smoothness cost is removed, the robot occasionally exhibits a back-and-forth motion of the flippers during traversal. This motion increases both the traversal time and rot. ang. compared to the full cost function. This observation suggests that the smoothness cost helps reduce unnecessary movements and improves traversal efficiency.

C. Multi-Terrain Traversal in Real-World Scenarios

We deploy the terrain traversal system on the Searcher robotic platform to conduct experiments in real-world scenarios, as shown in the supplemental video, to demonstrating that our approach can traverse multiple terrains in succession. Fig. 9 shows a collection of screenshots from one of the experiments, a scenario involving a high platform and staircases. As expected, HTO module successfully generates the hybrid motion and the controller can track the reference trajectory, as shown in Fig.10.

1) Results of Mode Switching: Fig.10 shows that the HTO module is capable of generating motion with mode switching in a multi-terrain traversal. Specifically, the robot successfully climbs up the high platform by switching to traversing mode within 18-29s. Each staircase's traversal undergoes two traversal modes and one driving mode since the steps are simplified to a plane and the planner regards the robot as driving on a plane when the body is entirely situated on it. A short driving mode occurs during 129-131s due to the stairs' brief length.

2) Tracking Performance: The planned trajectory and measurements show that the controller has excellent tracking performance, as evidenced by the mean absolute tracking errors with standard deviations along the entire traversal, which are as follows: s_d: 3.09 ± 5.80 (cm), s_t: 2.74 ± 4.28 (cm), θ_f: 1.31 ± 1.96 (deg), and θ_r: 1.78 ± 2.40 (deg).

3) Comparison with Operator Control: We realize that there are differences in performance between the physical platform and the simulated robot. Additionally, successive traversal tasks are demanding for the operator, which

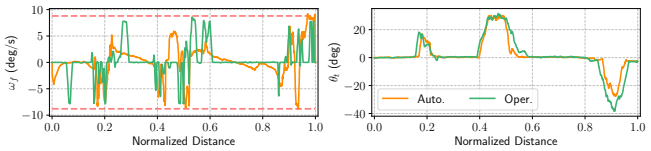

Fig. 11. Autonomous, operator-controlled terrain traversal of the front flipper speed, pitch angle along the normalized distance. The flipper velocity limit is indicated by the red line.

may lead to diverse strategies. Therefore, we also conduct experiments with the expert operator's traversal in the same scenario. The average time taken by oper. is 174.6s, compared to 152.1s for auto. The operator exhibits more caution, often pausing the robot to adjust the flippers for stability, resulting in longer traversal times. Fig. 11 shows the front flipper velocity and the pitch angle versus distance traveled. The auto. exhibits consistently smooth flipper velocities, seldom reaching their limit. In contrast, the operator has difficulty finely controlling the flipper velocities, necessitating repeated adjustments and causing the flippers to consistently move at maximum velocity. For pitch angle, the trends and magnitudes of the two methods in the first two terrains are similar. During stair descent, the maximum pitch angle of auto. (27.7deg) is even lower than oper.'s (38.4deg) due to the different strategies, showing higher stability. The experiments validate the capability of our approach to traverse through multiple terrains more swiftly and with enhanced stability, surpassing that of the operator.

VI. Conclusion and Future Work

To the best of our knowledge, this work is the first application of trajectory optimization techniques to articulated tracked robots for terrain traversal. We present a planar RTI model that facilitates the configuration description of the robot interacting with the terrain. A novel HTO problem formulation, transcribed into a multi-objective NLP, is solved in real-time to generate motions with hybrid mode switching between driving and traversing. In addition, a terrain traversal system containing map sampling, terrain simplification, HTO, and a tracking controller is designed and deployed. Our approach is validated on both simulated and physical platforms, outperforming human operator control in terms of motion smoothness, stability, and efficiency. Future work will focus on global path planning based on online mapping to further increase the autonomy of the system to perform full-stack autonomous navigation and complex tasks.

References

[1] T. Klamt, D. Rodriguez, L. Baccelliere, X. Chen, D. Chiaradia, T. Cichon *et al.*, "Flexible disaster response of tomorrow: Final presentation and evaluation of the centauro system," *IEEE Robot. Autom. Mag.*, vol. 26, no. 4, pp. 59–72, 2019.

[2] N. Michael, S. Shen, K. Mohta, Y. Mulgaonkar, V. Kumar, K. Nagatani *et al.*, "Collaborative mapping of an earthquake-damaged building via ground and aerial robots," *J. Field Robot.*, vol. 29, no. 5, pp. 832–841, 2012.

[3] F. Niroui, K. Zhang, Z. Kashino, and G. Nejat, "Deep reinforcement learning robot for search and rescue applications: Exploration in unknown cluttered environments," *IEEE Robot. Autom. Lett.*, vol. 4, no. 2, pp. 610–617, 2019.

[4] S. Steplight, G. Egnal, S.-H. Jung, D. B. Walker, C. J. Taylor, and J. P. Ostrowski, "A mode-based sensor fusion approach to robotic stair-climbing," in *IEEE Int. Conf. Intell. Robots Syst.*, vol. 2. IEEE, 2000, pp. 1113–1118.

[5] K. Ohno, S. Morimura, S. Tadokoro, E. Koyanagi, and T. Yoshida, "Semi-autonomous control system of rescue crawler robot having flippers for getting over unknown-steps," in *IEEE Int. Conf. Intell. Robots Syst.* IEEE, 2007, pp. 3012–3018.

[6] Y. Okada, K. Nagatani, K. Yoshida, S. Tadokoro, T. Yoshida, and E. Koyanagi, "Shared autonomy system for tracked vehicles on rough terrain based on continuous three-dimensional terrain scanning," *J. Field Robot.*, vol. 28, no. 6, pp. 875–893, 2011.

[7] M. Sokolov, I. Afanasyev, A. Klimchik, and N. Mavridis, "Hyperneat-based flipper control for a crawler robot motion in 3d simulation environment," in *IEEE. Int. Conf. Robot. Biomimetics*. IEEE, 2017, pp. 2652–2656.

[8] M. Pecka, V. Šalanskỳ, K. Zimmermann, and T. Svoboda, "Autonomous flipper control with safety constraints," in *IEEE Int. Conf. Intell. Robots Syst.* IEEE, 2016, pp. 2889–2894.

[9] A. Mitriakov, P. Papadakis, J. Kerdreux, and S. Garlatti, "Reinforcement learning based, staircase negotiation learning: simulation and transfer to reality for articulated tracked robots," *IEEE Robot. Autom. Mag.*, vol. 28, no. 4, pp. 10–20, 2021.

[10] F. Colas, S. Mahesh, F. Pomerleau, M. Liu, and R. Siegwart, "3d path planning and execution for search and rescue ground robots," in *IEEE Int. Conf. Intell. Robots Syst.* IEEE, 2013, pp. 722–727.

[11] K. Zimmermann, P. Zuzanek, M. Reinstein, and V. Hlavac, "Adaptive traversability of unknown complex terrain with obstacles for mobile robots," in *IEEE Int. Conf. Robot. Autom.* IEEE, 2014, pp. 5177–5182.

[12] T. Azayev and K. Zimmermann, "Autonomous state-based flipper control for articulated tracked robots in urban environments," *IEEE Robot. Autom. Lett.*, vol. 7, no. 3, pp. 7794–7801, 2022.

[13] Y. Yuan, L. Wang, and S. Schwertfeger, "Configuration-space flipper planning for rescue robots," in *IEEE Int. Symp. Safety Security Rescue Robot.* IEEE, 2019, pp. 37–42.

[14] Y. Yuan, Q. Xu, and S. Schwertfeger, "Configuration-space flipper planning on 3d terrain," in *IEEE Int. Symp. Safety Security Rescue Robot.* IEEE, 2020, pp. 318–325.

[15] V. S. Medeiros, E. Jelavic, M. Bjelonic, R. Siegwart, M. A. Meggiolaro, and M. Hutter, "Trajectory optimization for wheeled-legged quadrupedal robots driving in challenging terrain," *IEEE Robot. Autom. Lett.*, vol. 5, no. 3, pp. 4172–4179, 2020.

[16] A. W. Winkler, F. Farshidian, D. Pardo, M. Neunert, and J. Buchli, "Fast trajectory optimization for legged robots using vertex-based zmp constraints," *IEEE Robot. Autom. Lett.*, vol. 2, no. 4, pp. 2201–2208, 2017.

[17] A. W. Winkler, C. D. Bellicoso, M. Hutter, and J. Buchli, "Gait and trajectory optimization for legged systems through phase-based end-effector parameterization," *IEEE Robot. Autom. Lett.*, vol. 3, no. 3, pp. 1560–1567, 2018.

[18] E. Jelavic and M. Hutter, "Whole-body motion planning for walking excavators," in *IEEE Int. Conf. Intell. Robots Syst.* IEEE, 2019, pp. 2292–2299.

[19] M. Posa, C. Cantu, and R. Tedrake, "A direct method for trajectory optimization of rigid bodies through contact," *Int. J. Robot. Res.*, vol. 33, no. 1, pp. 69–81, 2014.

[20] M. Bjelonic, P. K. Sankar, C. D. Bellicoso, H. Vallery, and M. Hutter, "Rolling in the deep–hybrid locomotion for wheeled-legged robots using online trajectory optimization," *IEEE Robot. Autom. Lett.*, vol. 5, no. 2, pp. 3626–3633, 2020.

[21] W. Wang, L. Zhou, Z. Du, and L. Sun, "Track-terrain interaction analysis for tracked mobile robot," in *IEEE/ASME Int. Conf. Adv. Intell. Mechatronics*. IEEE, 2008, pp. 126–131.

[22] Y. Liu and G. Liu, "Track–stair interaction analysis and online tipover prediction for a self-reconfigurable tracked mobile robot climbing stairs," *IEEE/ASME Trans. Mechatron.*, vol. 14, no. 5, pp. 528–538, 2009.

[23] Y. Chen, Z. Xu, Z. Jian, G. Tang, L. Yang, A. Xiao *et al.*, "Quadruped guidance robot for the visually impaired: A comfort-based approach," in *IEEE Int. Conf. Robot. Autom.* IEEE, 2023, pp. 12 078–12 084.

[24] M. Kelly, "An introduction to trajectory optimization: How to do your own direct collocation," *SIAM Review*, vol. 59, no. 4, pp. 849–904, 2017.

[25] M. Gianni, F. Ferri, M. Menna, and F. Pirri, "Adaptive robust three-dimensional trajectory tracking for actively articulated tracked vehicles," *J. Field Robot.*, vol. 33, no. 7, pp. 901–930, 2016.

[26] J. A. Andersson, J. Gillis, G. Horn, J. B. Rawlings, and M. Diehl, "Casadi: a software framework for nonlinear optimization and optimal control," *Math. Program. Comput.*, vol. 11, pp. 1–36, 2019.

[27] L. T. Biegler and V. M. Zavala, "Large-scale nonlinear programming using ipopt: An integrating framework for enterprise-wide dynamic optimization," *Comput. Chem. Eng.*, vol. 33, no. 3, pp. 575–582, 2009.

[28] W. Xu, Y. Cai, D. He, J. Lin, and F. Zhang, "Fast-lio2: Fast direct lidar-inertial odometry," *IEEE Trans. Robot.*, vol. 38, no. 4, pp. 2053–2073, 2022.

[29] M. Pecka, K. Zimmermann, and T. Svoboda, "Fast simulation of vehicles with non-deformable tracks," in *IEEE Int. Conf. Intell. Robots Syst.* IEEE, 2017, pp. 6414–6419.